JGR Space Physics

RESEARCH ARTICLE
10.1029/2022JA031208

Modeling Features of Field Line Resonance Observable by a Single Spacecraft at Saturn

T. Elsden[1] **and D. J. Southwood**[2]

[1]School of Mathematics and Statistics, University of St Andrews, St Andrews, UK, [2]Blackett Laboratory, Imperial College London, London, UK

Key Points:

- Simulation results are used to test and validate the interpretation by Southwood et al. (2021, https://doi.org/10.1029/2020JA028473) wave observations at Saturn
- The spatial phase structure in field line resonances can shift the observed frequency on a moving spacecraft between in/outbound passes
- We highlight how such frequency changes can be accounted for in both the spacecraft and simulation data

Supporting Information:

Supporting Information may be found in the online version of this article.

Correspondence to:

T. Elsden,
te55@st-andrews.ac.uk

Citation:

Elsden, T., & Southwood, D. J. (2023). Modeling features of field line resonance observable by a single spacecraft at Saturn. *Journal of Geophysical Research: Space Physics*, *128*, e2022JA031208. https://doi.org/10.1029/2022JA031208

Received 5 DEC 2022
Accepted 4 MAR 2023

Author Contributions:

Conceptualization: T. Elsden, D. J. Southwood
Data curation: D. J. Southwood
Formal analysis: T. Elsden, D. J. Southwood
Funding acquisition: T. Elsden
Investigation: T. Elsden, D. J. Southwood
Methodology: T. Elsden, D. J. Southwood
Project Administration: T. Elsden, D. J. Southwood
Software: T. Elsden
Validation: T. Elsden
Visualization: T. Elsden

Abstract The observations of Southwood et al. (2021, https://doi.org/10.1029/2020JA028473), using data from the Cassini magnetometer from the final (proximal) orbits of the mission at Saturn, show large scale azimuthally polarized magnetic signals are always present near periapsis. The signals were attributed to standing Alfvén waves excited on the magnetic shells planetward of the Saturn D-ring. The apparent absence of any systematic variation in frequency as the spacecraft crossed magnetic shells, implied that the signals were not simply locally excited standing Alfvén modes, but were pumped by coupling to global compressional eigenmodes excited in a cavity formed in the dayside magnetosphere. In this study, we use a numerical magnetohydrodynamic (MHD) model to test such theoretical explanations for the observations, by examining in detail the MHD wave coupling and large scale spatial structure of the signals. The modeling not only shows good agreement with the data but further provides new insight into features previously overlooked in the data. In particular, we show how the apparent frequency of a single spacecraft observation is affected by the phase variation present in a local field line resonance.

Plain Language Summary On the final orbits of the Cassini Saturn Orbiter, one surprise was the discovery of large magnetic oscillations perpendicular to the background planetary field. The disturbances were present each time the spacecraft passed planetward of the innermost rings. This study models what a spacecraft would see if the signals were large scale magnetohydrodynamic waves excited within a high-density plasma. The strong alignment of the magnetic oscillations transverse to the background led to the original proposal that the signals are highly localized Alfvén waves in what is known as field line resonance. The simulations, however, reveal subtle aspects of the overall picture and how the system is being excited. In particular, it is shown that on the quasi-polar orbits such as Cassini followed one expects some unexpected features, such as the signal frequency detected in the largest field component differs between hemispheres. Moreover, the frequency detected on the spacecraft might substantially differ in field components in different directions. The conclusion that the signals are resonantly excited Alfvén waves hold up but the simulations show that such excitation must have a complicated spatial amplitude and phase structure. A re-examination of the Cassini data has revealed some of the effects discovered in the computer simulations.

1. Introduction

Ultra-low frequency (ULF) magnetic field oscillations have been observed at Earth for over 150 years (Stewart, 1861). These are attributed to large scale magnetohydrodynamic (MHD) waves set up in the magnetosphere. Other planets of the solar system with strong intrinsic magnetic fields (Glassmeier & Espley, 2006 and references therein) also sustain such large-scale waves. These waves transport energy and momentum in the magnetospheric system. The waves can reveal important information about the magnetospheric structure (e.g., magnetic field and plasma density properties, e.g., Denton et al., 2006; Takahashi et al., 2006). On Earth, there exists a plethora of ground and space-based instrumentation to observe the ULF band. Indeed, most modern observational studies involve data from a suite of spacecraft in conjunction with ground magnetometers or radars to provide extra evidence for the interpretation of the data (e.g., Shi et al., 2018). On the other planets, however, normally measurement is made from a single spacecraft, making the interpretation of such data challenging due to the ambiguity associated with separating spatial and temporal effects. In this study, we use the extensive knowledge of MHD waves gleaned from ULF studies on Earth, together with high-resolution MHD simulations to assist in the interpretation of satellite measurements of ULF oscillations detected at Saturn.

Writing – original draft: T. Elsden, D. J. Southwood
Writing – review & editing: T. Elsden, D. J. Southwood

Southwood et al. (2021) reported observations of such low-frequency signals (periods ∼1 − 10 min) in Saturn's magnetosphere from the Cassini magnetometer during the final 22 (proximal) orbits of the mission. At periapsis, the spacecraft passed planetward of Saturn's inner D-ring. During this phase of each orbit, large-scale azimuthally polarised magnetic signals were *always* present, suggesting a systematic steady state rather than some transient phenomena. The signals were attributed to standing Alfvén waves excited on the magnetic shells planetward of the Saturn D-ring. There was furthermore an apparent lack of any systematic variation in the frequency as the spacecraft crossed magnetic shells, as would be expected of locally excited standing Alfvén modes. The frequency would usually be expected to increase moving radially inward, in line with an increasing Alfvén speed caused by an increasing magnetic field strength as well as moving to shorter field lines. This led the authors to infer that the signals were pumped at a coherent frequency. Such a frequency could be enforced by global compressional eigenmodes excited in a cavity/waveguide formed in the dayside magnetosphere, which represents a theory of MHD wave-coupling employed for several decades at Earth (Kivelson & Southwood, 1985, 1986; Samson et al., 1992).

The goal of this work is to use numerical simulations to model these oscillations in Saturn's inner magnetosphere and to identify which features that appear in the modeling are detectable in the data. Although motivated by data obtained at Saturn, our work illuminates the dynamics of the MHD wave modes in a cold plasma and has general relevance to in-situ measurements of MHD waves in any magnetosphere. We continue this introduction by discussing the details of the observations of Southwood et al. (2021), followed by an appropriate introduction to the theoretical and modeling considerations.

1.1. Observational Motivation

Figure 1 is based on the data shown in figure 15 by Southwood et al. (2021). The top panel shows the band-limited (filtered between 1 and 5 min periods) azimuthal magnetic field component ΔB_ϕ with a period of ∼176 s, observed as the Cassini spacecraft penetrates magnetic shells planetward of the innermost D-ring on Cassini Orbital Revolution (Rev) 291 on 02 September 2017 between 12:50:25 and 13:25:41 UT. The Saturn planetary magnetic field is axisymmetric and so magnetic shells can be characterized by the radial distance of the point where they are furthest from the planet, or equivalent L shell (EqL, measured in Saturn radii). The L shell of the spacecraft is shown in the lower panel. Time, T, is measured from when the innermost shell is encountered at L = 1.03. The blue and red portions of the trace denote when the spacecraft is traveling inbound and outbound respectively. The spacecraft is on shells that thread the innermost Saturn ring, the D-ring when $1.24 > L > 1.11$. The orbit is such that, near periapsis, at the same time before and after the innermost magnetic shell, it is on the same magnetic shell. One can see that the signals rise above the background (which has been subtracted) as the spacecraft crosses the D-ring shells inbound (~ -850 s $< T < -528$ s) and then decay on crossing the D-ring shells outbound (~ 528 s $< T < 850$ s). Peak amplitudes are detected in the 1.5 cycles shown in the shaded segments between $T = \pm 264$ s and ± 528 s. Between in and outbound encounters with the signals, the spacecraft has changed hemispheres. The observations, therefore, suggest that the entire flux tubes must be oscillating and likely have a standing structure along the background field. Nonetheless, as we shall see, there is some subtlety in interpreting what is seen.

Signals like those shown in Figure 1 are detected on each of the proximal orbits. The proximal orbits take the spacecraft planetward of the rings. Although the orbits are highly inclined, they are not quite north-south symmetric. On any given pass planetward of the D-ring, the spacecraft moves from north to south crossing around 40° in latitude in just under 2 hr in local time (LT). Periapsis is reached just below the equator. Although the Saturn field is axisymmetric, the field is not north-south symmetric (Dougherty et al., 2018). Southwood et al. (2021) define the equivalent magnetic equator as where the radial component of the background field is zero. This is normally encountered just above the planetary equator. In Figure 1, the spacecraft crosses this point on the orbit when $T = -105$ s. The wave field is in fact zero at this point.

There is a high mass density in the region planetward of the rings although uncertainties remain regarding this. That the densities of positively charged ions do not match the observed electron densities shows this gap in knowledge (Morooka et al., 2019). Morooka et al. (2019) explained the discrepancy by the presence of unknown quantities of positively or negatively charged dust. It does mean that the plasma mass density is not known precisely. Indeed, further theoretical work on the basis of the spectrum of waves seen could shed light on the effective mass density of the local plasma in the regions through which the spacecraft is moving.

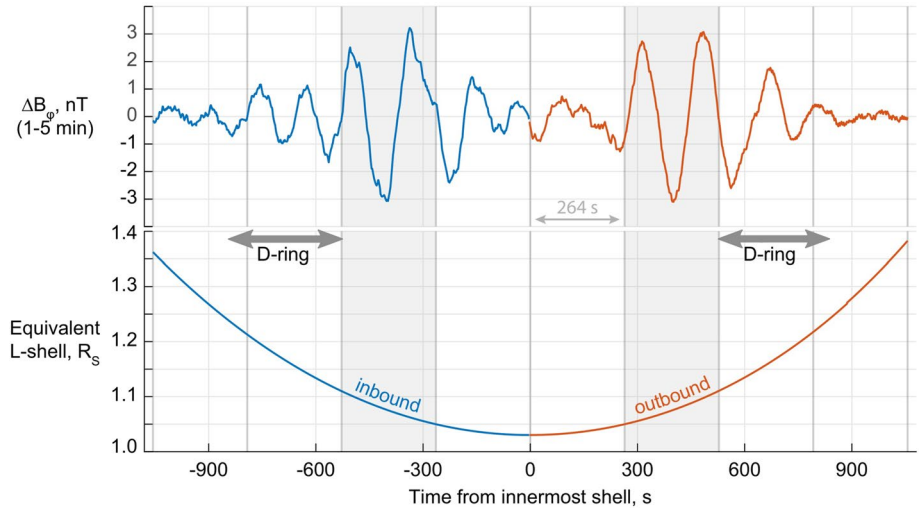

Figure 1. Reproduced from figure 15 of Southwood et al. (2021). The top panel shows band-limited signals of the azimuthal magnetic field perturbation ΔB_ϕ with period near 176 s. A 1–5 min period filter has been applied. The lower panel shows the magnetic shell of the spacecraft, on Cassini orbit Rev 291. The *x*-axis in both panels is time, T, measured in seconds from when the spacecraft encounters the innermost magnetic shell (EqL = 1.03, further explained in main text). Trace colors are blue before the innermost shell encounter and red after. The shaded regions correspond to when the spacecraft is crossing magnetic shells with 1.05 < EqL < 1.11 inbound (left) and outbound (right). The vertical lines are separated by 264 s. The magnetic shell at the D-ring inner edge is crossed at T = ±528 s, with the outer D-ring edge crossed at T ~±850 s, as indicated by the thick gray arrows.

1.2. Theory and Modeling Considerations

The signals of the previous section are seen on all 22 orbits. The large amplitude azimuthal signals appear out of background noise as the spacecraft crosses the magnetic shells threading the D-ring and enters a high-density plasma that could be regarded as the topside ionosphere. The presence of the signals on all orbits implies that they represent a steady-state process.

A further critical property of the signals is the lack of frequency variation with L-shell. This occurs in spite of the resonant Alfvén mode eigenfrequency varying significantly with L-shell, which varies due to the changing magnetic field geometry, as well as likely changes in plasma mass density, magnetic field strength, and field line length with radial distance. Therefore, if the field lines were freely oscillating at their natural frequencies in response to a broadband driver, one would expect to see such a frequency variation as the spacecraft crossed L shells. Instead, there are band-limited frequencies present in this region inside of the D-ring shell. This led Southwood et al. (2021) to suggest that the narrow band response meant that the local azimuthally polarised waves were being driven by energy fed from global fast eigenmodes. The works of Kivelson and Southwood (1985, 1986) introduced the concept of global magnetohydrodynamic (MHD) eigenmodes of Earth's dayside magnetosphere, in order to explain the discrete band-limited frequency signals often observed. Global modes are fast MHD waves that are inherently damped through the coupling between the fast MHD mode and the Alfvén mode. At the lowest frequencies, the Alfvén mode adopts a standing structure along the field and its eigenfrequencies vary from magnetic shell to shell. Each oscillating shell is known as a field line resonance (FLR) (Southwood, 1974). The global fast eigenmode damping is caused by the FLRs, due to energy being irreversibly transferred from the fast to the local Alfvén wave. When significant dissipation is present (i.e., through a resistive ionosphere), the steady state resonance exists over a finite L shell width (Mann et al., 1995).

A global fast mode with a consistent frequency in the observed region could explain the data in two ways. First, if there is no local FLR, coupling far away can introduce an Alfvén mode component into a global eigenmode. However, the amplitude of such signals would not be very large as they are not resonant oscillations. A priori this seems unlikely in the Cassini observations. The transverse azimuthal oscillations have amplitudes as much as an order of magnitude larger than the components in the meridian, which would correspond to the global fast mode polarisation. Second, with strong dissipation causing a broader bandwidth, one finds a relatively large FLR width (Mann et al., 1995), thus allowing a large amplitude narrow band Alfvén mode excitation over a finite range of magnetic shells. We shall investigate these possibilities further here and compare them with observations.

A new issue specifically raised in this study is the effect of spacecraft motion. The fast-Alfvén wave coupling that gives rise to FLR inherently introduces spatial phase structure in the vicinity of the resonant shell. Spatial phase variation can appear as time variation in phase, that is, a modification of the frequency, on a spacecraft moving through the structure. This was noted at Earth by Anderson et al. (1989); Takahashi et al. (1990), who showed evidence of frequency differences between inbound and outbound spacecraft passes of up to 15% at L ∼ 5. This has also been studied for low Earth orbit satellites, which are passing much more rapidly through the resonance (Heilig et al., 2013; Vellante et al., 2004), which enhances this effect. Indeed, this will be important for Cassini, given how quickly it passes through the region of interest. Sampling from a simulated spacecraft in our modeling provides key insight, as we will show. Thus, although motivated by observations in the Cassini data set used by Southwood et al. (2021), our numerical MHD modeling will also bring new perspectives on what can be observed by a spacecraft when traveling through a FLR, potentially useful in any magnetospheric context.

The paper is structured in the following way: Section 2 describes the numerical MHD model used for the simulations; Section 3 analyses the results from the simulations from a fundamental MHD wave coupling perspective; Section 4 considers the observational features of FLR by a spacecraft; Section 5 links the model and the data by analyzing virtual spacecraft signatures; Section 6 presents examples from the data to compare with the modeling. Conclusions are given in Section 7.

2. Numerical Model

The numerical model used will be briefly summarized here, though the interested reader should refer to the simulation development focused study for full details (Wright & Elsden, 2020). The model solves the resistive, linear MHD equations for a cold plasma in a background dipole magnetic field geometry. A key feature of the model is the development of a set of field-aligned orthogonal coordinates, based on optimizing the standard dipole coordinates for numerical efficiency. These new coordinates, labeled (α, β, γ), mitigate some of the grid spacing issues which arise when using dipole coordinates, leading to numerically inefficient codes. Such features are very well explained by Kageyama et al. (2006). The γ coordinate is along the field direction, β is in the azimuthal direction and α is in the direction of the local field outward normal, that is, it labels magnetic shells and in the equatorial plane coincides with the radially outward direction. The coordinate system is designed to be effective for studying the small-scale structure between magnetic shells, which occurs where the coupling between the fast compressional mode and the transverse Alfvén mode drives the latter into FLR.

The simulation domain and setup are shown in Figure 2. The dimensions of the simulation domain are not as extreme as the actual Kronian context where the observed signals are encountered on shells corresponding to dipole L = 1.03 − 1.24. For computational economy, the inner boundary of the simulation is placed at L = 1.2 as shown by the grid in the upper left panel (a) in Figure 2, displaying selected contours of the meridional (α) and field-aligned (γ) coordinates in the X-Z plane. Panel (b) displays the equilibrium Alfvén speed in the equatorial plane. The chosen separation into two cavities is clear, with the blue region representing the smaller dense inner cavity and the red representing the larger diffuse outer cavity. The density gradient marking the equivalent of the D-ring crossing is between L = 1.5 − 1.8, and the Alfvén speed transitions smoothly between the two regions. On either side of this transition, the Alfvén speed is held constant. Furthermore, there is no azimuthal variation in the Alfvén speed. The outer boundary of the computational domain is L = 4, which at Saturn, would approximately mark the orbit of Enceladus, so the scale of the actual dayside magnetosphere is substantially larger. However, as Enceladus is a primary source of plasma for the magnetosphere that diffuses outwards, the shells inside its orbit are likely to form an effective cavity for the fast MHD mode.

The inner boundary, the lower and upper ionospheric boundaries, and the boundaries in azimuth are all chosen to be perfectly reflecting. For the ionosphere, the assumption corresponds to perfect conductivity and for the inner boundary, it corresponds to a rigid boundary. The boundary in azimuth (local time) is the most unrealistic as it precludes azimuthal energy transport. Hence, the domain is a cavity rather than an open-ended waveguide. The azimuthal extent is limited to a quarter of the whole domain for numerical efficiency. As previously mentioned, it is the meridional structure that will govern the behavior and is of interest in this study. The simulation is driven from the outer boundary at L = 4, by perturbing the field-aligned magnetic field component b_γ at a fixed frequency, as described in the next section.

The simulations include dissipation through the magnetic diffusivity η, which has a uniform value throughout most of the domain. Close to the ionospheric end of the field lines, η is smoothly tapered to zero to prevent short

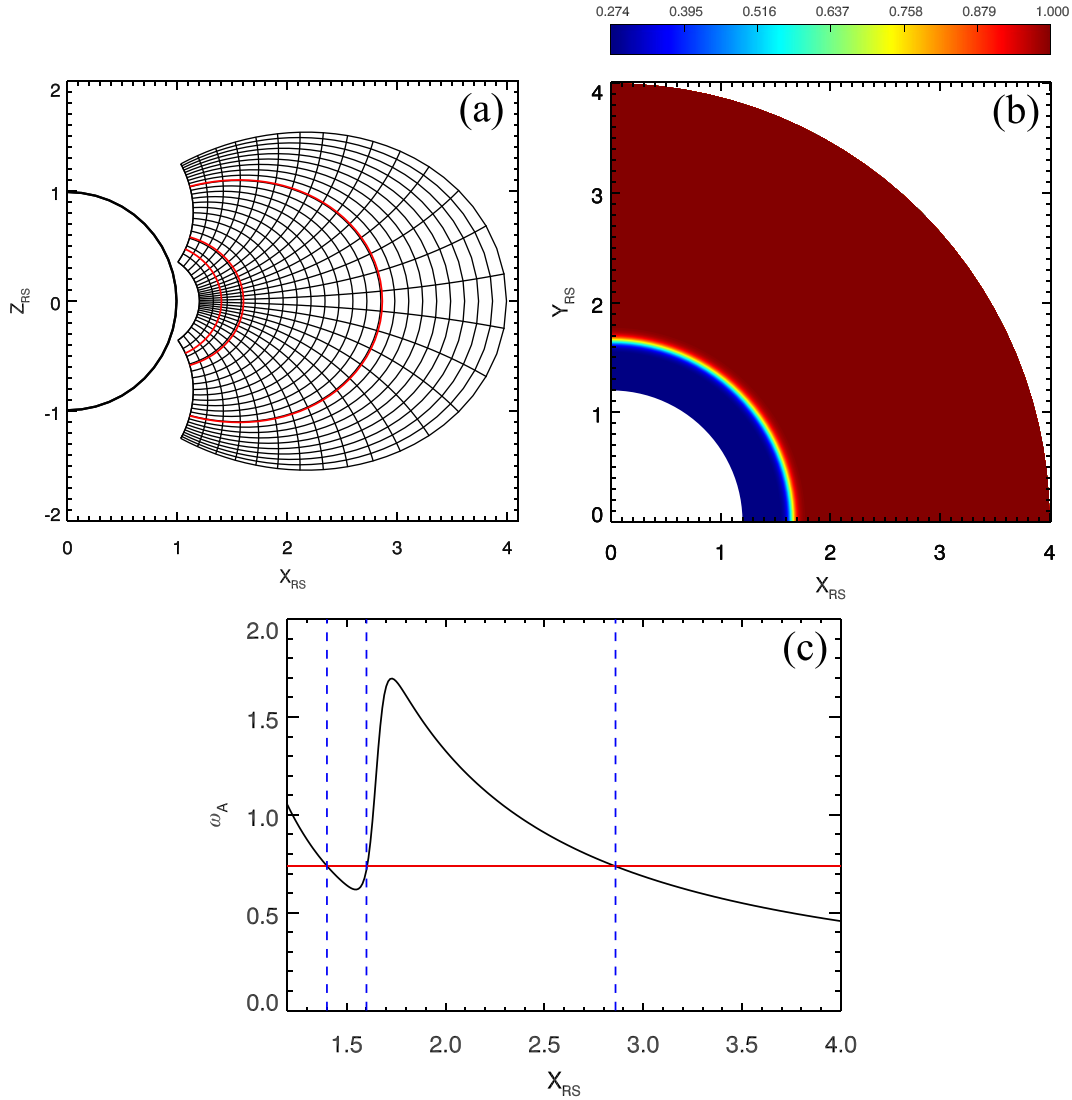

Figure 2. Simulation setup, (a) example coordinate grid for the simulation, displaying contours of the meridional and field-aligned coordinate (note: only every 13th contour across the field and every 2nd contour along the field are plotted). (b) Contour in the equatorial plane of the equilibrium Alfvén speed. (c) Alfvén frequency (ω_A) variation with radius. Solid red line denotes the driving frequency, dashed vertical blue lines give the locations where field line resonances are expected to form.

diffusion timescales in this region where the numerical grid spacing decreases. A full discussion of this is given in Section 3.4 of Wright and Elsden (2020). Dissipation is included in order to limit the radial width of FLRs such that it is always suitably resolved. The simulation code was tested extensively, with energy conserved typically to one part in 10^5.

The variation in the fundamental Alfvén frequency, ω_A, with equatorial radial distance is shown in panel (c) of Figure 2. In the regions where the Alfvén speed is constant, the variation in the field line length still provides a significant change in the frequency, resulting in a smooth Alfvén continuum. The most important effect of the increased density in the inner region is to provide a sharp change in the Alfvén speed between L = 1.5 and L = 1.8. In order to resolve the steep radial gradients in the resulting waves, the number of grid points used in each of the coordinate directions is $(\alpha_m, \beta_m, \gamma_m) = (420,30,60)$. The chosen driving frequency is denoted by the red line in Figure 2c. Where this frequency intersects the Alfvén frequency, FLRs are expected to form, as marked by the vertical blue dashed lines.

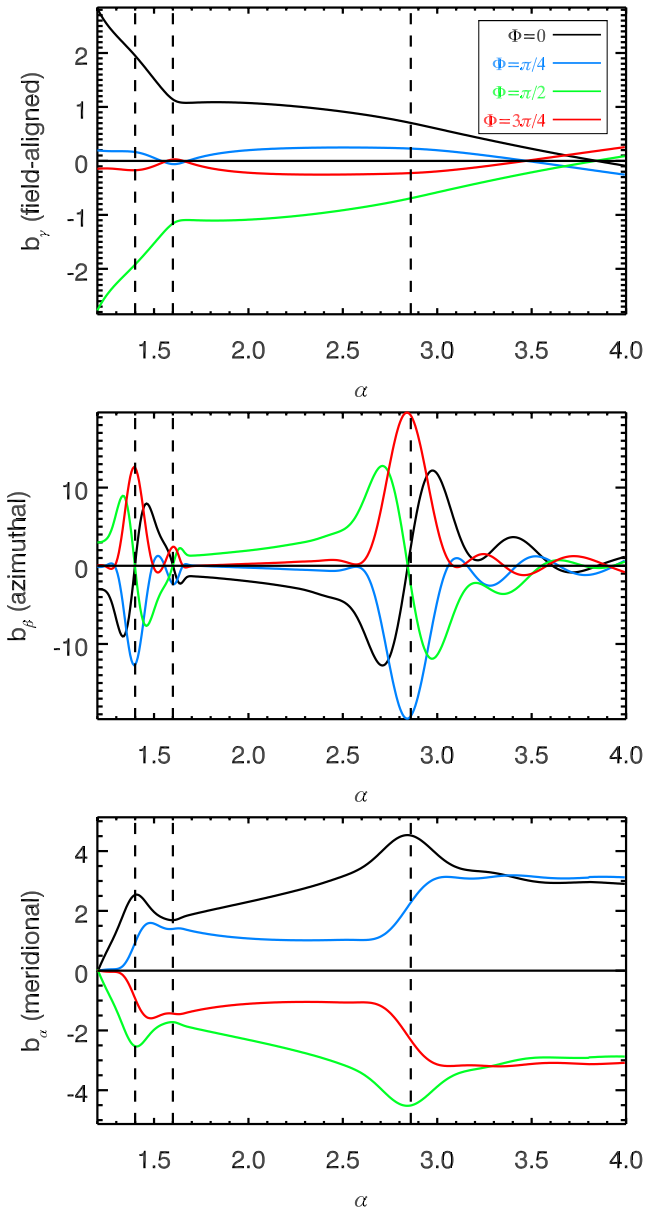

Figure 3. Radial dependence once the simulation has reached a steady state, of *Top* - Field-aligned magnetic field b_γ; *Middle* - Azimuthal magnetic field b_β; *Bottom* - Meridional magnetic field b_α. The colored lines correspond to different times separated by a quarter wave period in the order black, blue, green, and red. Vertical dashed lines denote expected field line resonance locations.

3. MHD Wave Coupling and System Behavior

Before considering matching the observations, we examine the overall behavior of the simulation system outlined in the previous section. A simple source is chosen in which the outer boundary surface at L = 4 is forced into oscillation with a fixed frequency. The frequency is chosen to be close to an eigenfrequency for the compressional mode in the cavity formed by the boundaries at L = 1.2 and L = 4. The magnetic compression enforced on the boundary is transmitted through the system as a meridional oscillation. With the boundary conditions detailed in the previous section, if there were no azimuthal variation, that is, azimuthal wave number $k_\beta = 0$, the wave components would exhibit secular growth over many cycles, as energy accumulates as the source pumps the meridional motion. Eventually, numerical dissipation would bring saturation, with dissipation distributed throughout the volume. If $k_\beta \neq 0$ however, the behavior is very different. The difference between the $k_\beta = 0$ and $k_\beta = 2$ (used here) cases is that once $k_\beta \neq 0$, the fast compressional mode couples to the MHD Alfvén mode and FLR occurs. The Alfvén mode FLRs provide highly localized energy absorption and energy balance between modes is established rapidly.

The driven boundary perturbation to the field-aligned magnetic field component imposed at L = 4 is

$$b_\gamma(\alpha = 4, \beta, \gamma, t) = \cos(k_\beta \beta)\cos(k_\gamma \gamma)\sin(\omega_d t), \quad (1)$$

for $k_\beta = m = 2$, $k_\gamma = \pi/(2\gamma_{\max})$ and driving frequency $\omega_d = 0.739$ (period $\tau_d = 8.502$; dimensionless values are presented for the simulations throughout). These values provide a half wavelength dependence azimuthally over the simulation domain ($0 < \beta < \pi/2$) and a half wavelength (the fundamental) along the field line. The fundamental cavity mode has a quarter wave structure in the meridian between the driven outer boundary and the rigid inner one.

Figure 3 illustrates the overall spatial profile of the three magnetic components once the system has reached a steady state, which occurs once energy inputted into the domain from the driven boundary is balanced by that dissipated through the inclusion of resistivity. It displays the radial dependence of each magnetic field component at four equally spaced phases, Φ, during a wave cycle where the time order is black (Φ = 0), blue (Φ = π/2), green (Φ = π), and red (Φ = 3π/2). The top panel shows the profile in the meridian of the compressional component, b_γ. The plot is taken at the equator and along the central meridian. The black and green traces resemble the quarter wave form one would expect for a pure eigenmode with a node of the radial velocity at the inner boundary and a node of b_γ at the outer driven boundary (Appendix A of Elsden and Wright (2015) showed that driving the boundary with magnetic pressure results in a node of the compressional field (b_γ) there). The traces half a cycle apart in time are a little different from the case where $k_\beta = 0$ (i.e., no mode coupling). However, the blue and red traces (in quadrature with the black and green) represent the difference with $k_\beta = 2$.

In the steady state, the signal phase in a pure eigenmode would not vary. The red and blue traces here represent an oscillation in quadrature with the black and green and would not be present in a pure eigenmode. At Φ = π/2 and Φ = 3π/2 in the cycle, the pure mode would be zero everywhere. The presence of the spatially varying small signals in quadrature with the primary b_γ signal means that the phase of the overall b_γ oscillations varies from magnetic shell to shell. Spatial phase structure has long been recognized as linked to energy transport in large-scale MHD waves (Southwood, 1975; Southwood & Kivelson, 2000). In this case, the mode coupling

induces irreversible energy transfer from the compressional mode to the Alfvén mode FLRs, and the small, in quadrature signals, are directly associated with the energy transfer toward the FLR shells.

A further feature is clear in the black and green profiles for the field-aligned component (top panel). At the density step at L ~ 1.6, the magnitude of the gradient in amplitude in the meridian changes dramatically. It results in an enhanced amplitude in the high-density region that peaks at the inner boundary. The effect can be seen as the direct result of there being a rigid inner boundary condition. The compressional signal can be thought of as pumping the transverse azimuthal signals, so the enhancement in the inner region contributes to the high transverse amplitudes there.

The middle panel in Figure 3 shows the azimuthal magnetic field, b_β. Despite the fact that this component would not be present at all if $k_\beta = 0$, the amplitude scale in the plot is now substantially larger than for the other components. With finite k_β the azimuthal variation of the compressional component is now pumping azimuthal motion. The azimuthal motion is most effectively excited at the FLR shells and it follows that the azimuthal component shows most clearly the Alfvén mode FLR behavior. The red and blue traces have peaks at the three shells where FLR occurs (where $\omega = \omega_A$ as indicated in the bottom panel of Figure 2). At the FLR locations, the azimuthal motion is being pumped by the gradients in b_γ, just as in an oscillator forced at its resonant frequency.

The azimuthal component (middle panel) also shows substantial black and green signals peaking on either side of the resonance. This means that the phase of the b_β oscillations changes substantially as one moves from shell to shell through resonance. As we shall discuss below, the sign change across the resonance in these traces implies a net change of π in phase across the resonant region and will have potentially important observational effects for a spacecraft moving through the FLR.

The meridional magnetic field component, b_α, transverse to the field is shown in the bottom panel of Figure 3. As with the other transverse component, b_β, the standing structure along the field means that it has a node at the equator. Therefore, the plot is taken from off the equator and in the central meridian. The b_α component has smaller amplitude at peak values than b_β. It is a hybrid signal; effects can be seen attributable to both wave modes. There is a large-scale background variation that reflects the dominant quarter wavelength mode structure of the fast mode in the meridian. At the inner rigid boundary, the MHD frozen field condition means b_α has a node there. At the outer boundary, where the system is driven, the plasma displacement in the α direction has an antinode (maximum), as does b_α. This confirms a previous statement, that driving the outer boundary with perturbations to the field-aligned magnetic field component b_γ, simulates a node of b_γ there (Elsden & Wright, 2015), hence the antinode in the meridional displacement.

Superposed on the large-scale variation of b_α there are also clear local amplitude increases at the FLR locations. A simple way to understand this is that when k_β is non-zero the b_α component is required to meet Gauss's law ($\nabla \cdot \mathbf{B} = 0$). In other words, the field lines of the large azimuthal FLR perturbation are closed close to the resonance in the plane perpendicular to the background field. Comparing the colors of the traces in the relevant plots of Figure 3 shows that near resonance, b_α is in spatial quadrature with b_β, as would be expected. For clarity, a movie showing this time dependence is included as supplementary information for this study (Movie S2).

4. Observable Features of Field Line Resonance

As Wright and Elsden (2016) showed, the polarization behavior through resonance can be complex. However, for our purposes, we can note that our motivating observations, with very large azimuthal field perturbations, indicate the small azimuthal wavenumber case is appropriate. The azimuthal component stands out in the simulations as manifesting the effect of FLR, not only in amplitude but also in phase, as is indicated by the local amplitude peaks in both the black/green and the red/blue traces in the FLR vicinity in Figure 3. Near resonance, we can approximate the variation of the azimuthal component b_β across the FLR magnetic shell by the function:

$$f(x) = \frac{1}{x + i\epsilon} \tag{2}$$

where ϵ is a constant and x is the radial coordinate (Kivelson & Southwood, 1986; Southwood, 1974). The real and imaginary parts of $f(x)$ are shown in the upper panel of Figure 4.

We first compare the top panel of Figure 4 with the middle panel of Figure 3, where the spatial variation of the azimuthal component b_β is shown. By taking the black trace (in Figure 4) as the real part and the red trace as

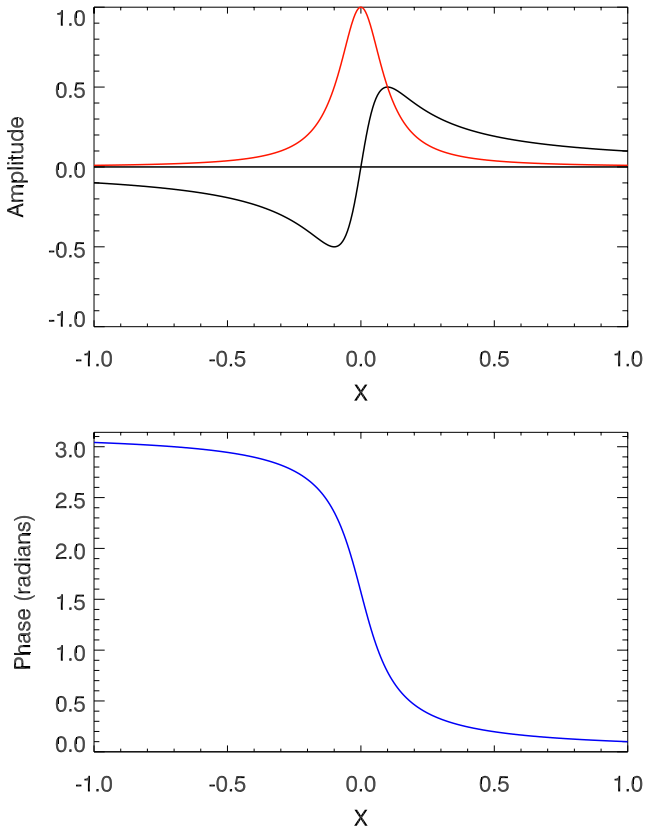

Figure 4. Idealized resonance structure. Top: Real (black) and imaginary (red) parts of the function $f(x)$ given by Equation 2. Bottom: Phase variation across the resonance that is, the argument of the complex function $f(x)$.

the imaginary part (i.e., lagging in phase by $\pi/2$), the function can be seen to reflect the relative variation of b_β through the resonance, as seen in the traces in Figure 3, if the resonance is located at $x = 0$. The lower panel of Figure 4 then shows the phase of the function $f(x)$ and thus allows picturing of the spatial phase variation from shell to the shell through resonance.

Any independent spatial variation evident between the black and red traces in Figure 3 means that there is an impact on phase. The black and red traces for the meridional components b_γ and b_α in the upper and lower plots do show distinct variation, meaning there is some spatial phase structure. However, there is nothing resembling the large phase change as seen in b_β. Accordingly, the main impact in the observations should be sought in the azimuthal component, b_β, for the small azimuthal wavenumber signals discussed here. In the b_β component, the overall change in phase through an individual resonance is π, potentially sufficient to cause a change in apparent frequency or even a change in sign of the oscillation amplitude. However, the observability will also depend on the speed of a spacecraft passage through the resonant shells as well as the parameter ϵ from Equation 2, which is related to the dissipation.

Figure 4 shows that the FLR structure would yield a change of order π across the scale of order a few times ϵ. ϵ is also the scale on which the amplitude of the resonance varies. Critical to detecting the effect of the phase change is the time a spacecraft takes to cross the resonance region, τ, say. When τ is comparable with the wave period, T, the spacecraft may detect up to half a cycle phase change (π) in one period, where the phase change should be 2π. According to the sign of the change, this would appear as a decrease in apparent frequency by a factor of two (negative phase change) or an increase by 3/2 (positive phase change). When $\tau \ll$T, the resonance is rapidly crossed; the oscillation component will simply exhibit a sign change in less than one cycle. When $\tau \gg$T, the spacecraft takes many wave periods to cross the resonance. The frequency change may be small but it will be modified over many cycles. Noting the phase change is much smaller in the meridional components, the most evident observational effect may well be a difference between the frequency observed in the azimuthal component and the meridional components.

We next examine how ϵ is parameterized. In Appendix A we provide a derivation of two Equations, A14 and A11, reproduced below as Equations 3 and 4. The equations show that the azimuthal displacement and magnetic field are controlled in the vicinity of resonance as.

$$\xi_\beta = \frac{1}{\left(\omega^2 - \omega_A^2(\alpha) + 2i\nu\omega\right)} \frac{B^2}{h_\beta \rho \mu_0} \frac{\partial}{\partial \beta}\left(\frac{b_\gamma}{B}\right), \tag{3}$$

$$\frac{b_\beta}{h_\beta} = \mathbf{B} \cdot \nabla\left(\frac{\xi_\beta}{h_\beta}\right), \tag{4}$$

(see appendix Equations A14 and A11) where h_β is a geometrical factor associated with the coordinate system ($h_\beta = r\sin\theta$ in spherical polar coordinates in an axisymmetric background field where the dipole is at the origin aligned along the symmetry axis) and ν represents damping or dissipation. As stated in Section 2, dissipation is included in the model through the magnetic diffusivity η. Of importance to the simulations is the time taken to establish an equilibrium, such that the resonances have achieved their steady-state amplitude, whereby energy fed to the resonance is balanced by that dissipated through Ohmic heating. The value of η is such that it takes approximately six periods to reach this steady state.

The resonant denominator is clear on the r.h.s. of Equation 3. The numerator is the azimuthal pressure gradient induced by the compressional component, b_γ. The plots in Figure 3 show that for the compressional component b_γ the phase change near resonance is small (compare the difference in amplitude of the black/red traces). Thus,

the denominator controls the phase variation in ξ_β (and b_β). Denoting the value of L on the resonant shell, L_0, we expand the expression for the resonant denominator in Equation 3 using a Taylor expansion to give:

$$\omega^2 - \omega_A^2(L) + 2iv\omega \approx 2iv\omega_A(L_0) - (L - L_0)\left[\frac{\mathrm{d}}{\mathrm{dL}}\left(\omega_A^2(L)\right)\right]_{L=L_0}. \quad (5)$$

Thus, the constant ϵ from Equation 2, measured in units of α (length) and expressed in terms of the system parameters is given by

$$\epsilon = \frac{v}{\left[\frac{\mathrm{d}}{\mathrm{dL}}(\omega_A)\right]_{L=L_0}}. \quad (6)$$

We now turn to the "observability" of resonances. The form of the resonant denominator in Equation 3 (and the expansion in Equation 5) shows that the resonant amplitude is inversely proportional to the radial gradient in FLR frequency, $\mathrm{d}\omega_A/\mathrm{d}\alpha$. This dependence is made explicit in equation (25) of Elsden and Wright (2017), where the resonance amplitude for a 3-D FLR is described. As we have just shown in Equation 6, the spatial scale of the resonance is also inversely proportional to the Alfvén frequency gradient (Mann et al., 1995). However, the wave amplitude will be greater at resonances where the Alfvén frequency gradient is shallower. Thus, although the most rapid spatial phase variation might appear to be where the gradient of ω_A is steepest, in circumstances where multiple resonances are occurring the equilibrium amplitude at the steepest gradient of ω_A is the weakest of the FLRs. This behavior is evident by comparing the resonance amplitudes in the middle panel of Figure 3 for b_β with the gradient of ω_A shown in the bottom panel of Figure 2 (the smallest resonance occurs in the steepest frequency gradient).

Finally, it must be noted that the sense of the phase change through resonance is also a function of the gradient in ω_A. When the radial gradient of ω_A is positive, as in the middle resonance of the three indicated in the lower panel in Figure 2, the phase increases inwards and so phase motion appears inwards. The resulting Doppler shift detected by an inward/outward moving spacecraft would cause a frequency decrease/increase respectively. The reverse would apply to the other two resonances in the lower panel of Figure 2 where the gradient of ω_A is negative. The spatial phase then decreases inwards and the resulting phase motion is thus outwards. The alternative way of thinking of this is that the phase motion is always in the direction of decreasing Alfvén frequency. Clear examples of this will be shown later such that this change can be more easily visualized.

4.1. Variation in Phase Along the Field

There is also a second effect to allow for the lowest frequency eigenmodes. The eigenmodes have an overall standing structure along the background magnetic field direction. Where there is north-south symmetry and where both ionospheres are reflecting, one expects the lowest frequency signals to have a node for the two transverse components (b_α and b_β) at the equator. The compressional component would have an antinode there. Thus, if a spacecraft travels through the equator the transverse signals would change sign (i.e., the phase changes by π).

The effect on the signal phase can be further complicated if the ionospheric boundaries are absorptive as that would introduce a phase variation along the background field (Newton et al., 1978). This can be complicated further by any asymmetries in the northern/southern ionospheric Pedersen conductances (Ozeke et al., 2005). These effects are not included here; nor have we seen evidence of this in the data referred to subsequently. However, the north-south phase difference is detected not only by the transverse signals passing through zero near the field equator but also in the phase differences detected in signals when the spacecraft passes the same magnetic shell inbound and outbound. Indeed, in our further discussion of the event shown in Figure 1, we shall point out this effect.

5. Virtual Spacecraft Signatures

We now consider how the effects present in the coupled global MHD eigenmode structure can impact observations made on a spacecraft passing through the signals. Figure 5 shows three separate cases, labeled 'a', 'b' and 'c', of spacecraft orbits through the simulation domain. The inbound portion of the orbits (from the north) is colored blue, with the outbound portion (to the south) colored red. The green and purple dashed lines represent

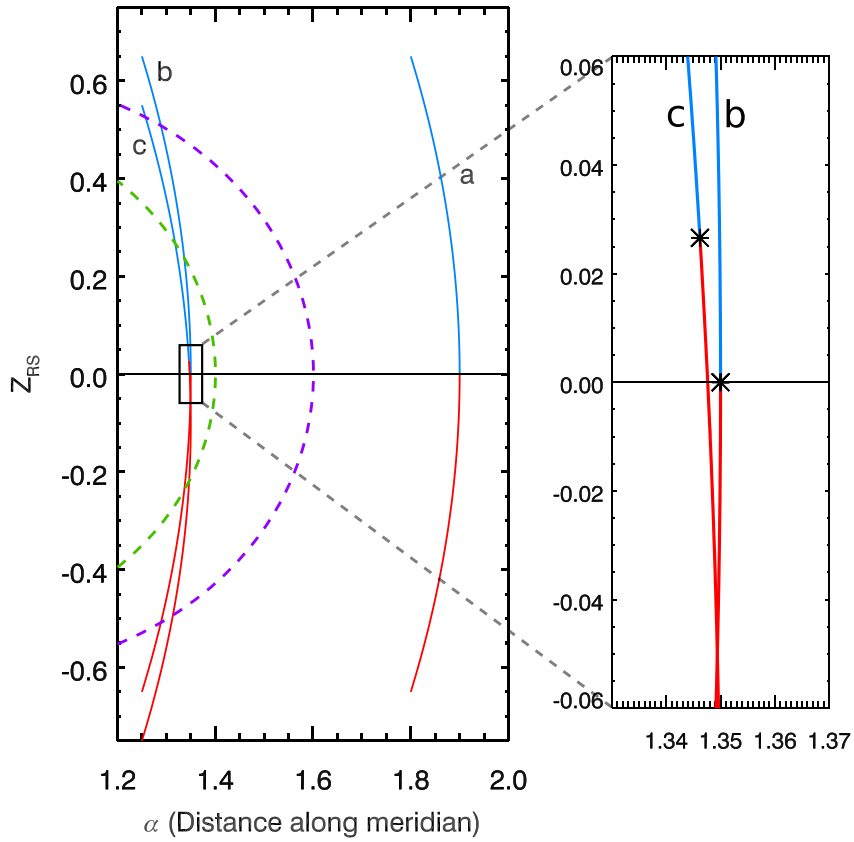

Figure 5. Three virtual satellite trajectories labeled 'a', 'b', and 'c' in a meridional plane along which fields are measured in the simulation domain to compare with data. Both 'a' and 'b' are north-south symmetric. Blue denotes the inbound and red the outbound phase of the orbit. The dashed green and purple lines represent the magnetic shells of the field line resonances located at $L = 1.4$ and $L = 1.6$ respectively. The expanded region shown to the right emphasizes the north-south asymmetry for orbit c, with asterisks marking the transition in the orbits from inbound (blue) to outbound (red).

the magnetic shells where FLRs are centered at L = 1.4 and L = 1.6. Orbit 'a' does not cross the FLR shells. Orbit 'c' is shifted to the south from orbit 'b' to study the north-south asymmetry present at Saturn due to the hemispheric asymmetry of the magnetic field. The expanded region shown to the right indicates how this has changed the portion of each orbit where the magnetic equator is crossed.

As mentioned in Section 3, the dimensionless driving frequency is $\omega_d = 0.739$ giving a period of $\tau_d = 8.502$. The speed of the spacecraft is chosen such that it takes just under 6 cycles (5.9) for the transit along the orbits shown. In the simulations, there will be a small azimuthal variation (as $k_\beta = 2$) due to the assumed standing structure in longitude. The satellite orbits are strictly in a meridional plane, ignoring any azimuthal motion of the spacecraft.

5.1. Spacecraft Orbit Missing the Resonance Region

The simplest case to consider is that where the spacecraft does not cross the central shells of an FLR, labeled 'a' in Figure 5. The top panel of Figure 6 shows the azimuthal magnetic field b_β as measured by a spacecraft moving uniformly along this trajectory from the North.

In all panels in Figure 6, a dashed black constant amplitude sinusoidal guide signal is shown. It represents the signal at a fixed point in the plasma frame of reference and we will refer to it simply as the 'guide'. We shall use it as a reference to show how motion-induced phase and amplitude changes occur in the observed signal. The solid vertical line marks the innermost shell encounter, which for this orbit coincides with crossing the magnetic equator. Comparing the solid and dashed traces one sees that the spacecraft signal comes to zero and changes sign (phase jump of π) at the equator, that is, it is passing through a magnetic node, consistent with the expected field-aligned nodal structure for the transverse field in the lowest frequency eigenmode. The mode structure along

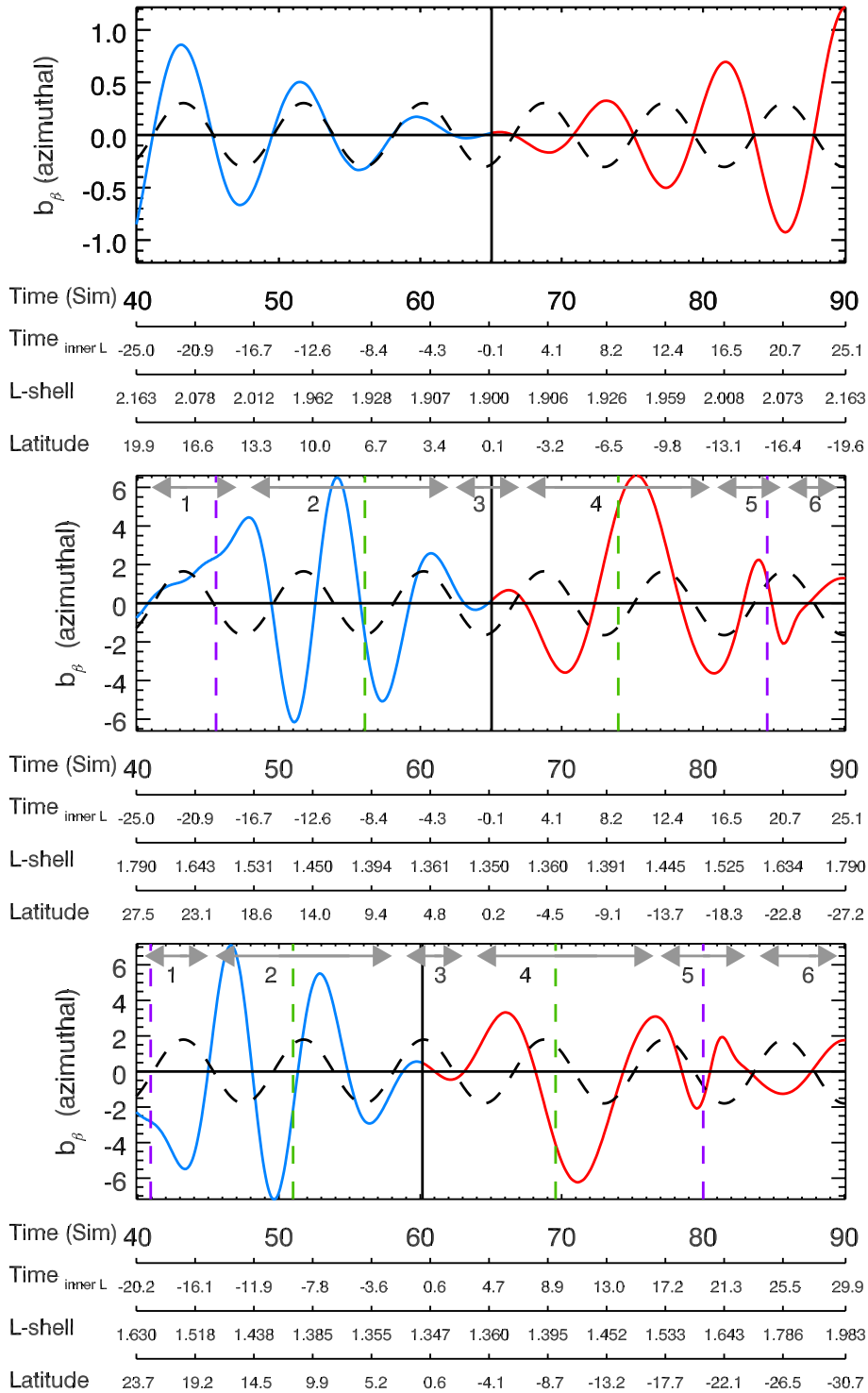

Figure 6. Time series (in simulation (sim) time units) of the azimuthal magnetic field component b_β measured along each of the trajectories from Figure 5 (top panel is the orbit labeled 'a' in Figure 5; middle is 'b'; bottom is 'c'). Blue is the inbound phase of the orbit, red the outbound. The dashed line is a constant frequency reference signal to highlight the phase structure. The vertical solid line represents the time when the spacecraft switches from the inbound to outbound phase of the orbit. The corresponding L-shell, latitude and time from the innermost L-shell are given as secondary axes below each panel. The purple/green dashed lines in the lower panels indicate where the spacecraft is crossing the field line resonance at $L = 1.6/\mathrm{L} = 1.4$ respectively. The gray numbered arrows in the lower panels demarcate time periods further explained in the main text.

the field also accounts for the amplitude increasing away from the equator crossing. The phase jump at the equator means that there is one wave cycle about the equator where, although the amplitude is small, the wave cycle appears to halve in length simply due to the presence of the node. However, the precise shape of the wave detected on equatorial passage depends on the phase of the signal when the spacecraft reaches the equator. Once the spacecraft is across the equator, the change in signal phase by π means that the oscillations are in antiphase with the guide sinusoid.

5.2. Spacecraft Orbit Encountering FLRs

The middle and bottom panels of Figure 6 show the signals recorded along the two orbits labeled 'b' and 'c' in Figure 5. The distinction between the orbits is that in orbit 'b', the innermost shell is encountered at the equator while orbit 'c' encounters the innermost shell in the southern hemisphere after it has passed through the equator. The latter geometry is very close to the actual Cassini proximal orbits. For the simulation, the spacecraft is assumed to move at a constant speed along the orbit and the speed has been chosen to display well the effect of resonance. In fact, the steady speed near periapsis does match what is seen near the Cassini periapses in practice.

The first remark is that even in orbit 'b' which is symmetric about the equator, crossing the resonance introduces significant departures from symmetry. However, by bearing in mind both the nature of the phase and amplitude structure through resonance as described earlier, along with the overall North–South asymmetry about the equator, the behavior of the signal (which we refer to as the 'trace') can be elucidated. In each panel the plots are divided into numbered time segments, 1–6, marked on the upper part of each plot and indicated by the gray double-headed arrows. We shall take each segment in sequence, beginning with orbit 'b' (middle panel).

In segment 1 of orbit 'b', the spacecraft is approaching the outer resonance in the steep density gradient inbound. The steep positive gradient, $d\omega_A/dL$, means that the resonance is thin. The resonance phase change causes the frequency to be reduced, and the resonance amplitude itself is small compared with the inner resonance. The zero in both the guide and trace at the beginning of the segment indicates that the guide and trace enter the resonance region in phase. The resonance is crossed where there is a zero in the guide signal (indicated by the purple dashed line). At the resonance, the trace should be in quadrature with the guide signal and so at peak amplitude. However, this is only just perceptible in the trace by a slight glitch. The reason is that the larger amplitude of the broader inner resonance is already affecting the trace as we enter segment 2.

Segment 2 begins with the trace having a peak, close to being in antiphase with the guide signal and ends with the trace close to in phase. The broader nature of the inner resonance is clear and its larger overall amplitude means it has primary influence over the trace for well over a cycle of the guide signal. There are ∼1.5 cycles of the guide whilst the trace completes two cycles in the segment. Thus the apparent signal frequency is increased by a factor of 4/3. This frequency increase is caused by the outward phase motion of the resonance combined with the inward spacecraft motion. The crossing of the inner resonance (green dashed marker) happens at a trough in the guide and the trace has a zero there. There are amplitude peaks in magnitude (one peak, one trough) at just over ∼1/4 cycle of the guide signal. Segment 2 ends with the trace more or less back in phase with the guide.

Segment 3 is where the equator is crossed and lasts a half cycle of the guided wave during which time the trace performs a 'wiggle' in each direction to reverse phase with respect to the guide. The equator crossing is close to a trough in the guide thus in this case the wiggle is first negative then positive once the equator is crossed. As the effect of the resonance is now weak, the wiggle resembles that seen on orbit 'a', first negative, then positive.

Segment 4 covers much of the inner resonance outbound. The apparent frequency of the trace is now ∼20% below that of the guide. This is caused by the opposite effect from the inbound portion, namely outbound spacecraft motion combined with outward phase motion in the resonance. Hence the phase structure is observed to pass more slowly across the spacecraft. A trough in the trace before the resonance is followed by a large peak shortly after resonance that occurs almost precisely in quadrature with the guide, as occurred inbound. The amplitude of the peak is very similar to the inbound seen 2.5 guide cycles earlier also near the resonance. The two trace troughs in the segment are of similar magnitude despite the first being much closer to the resonance. The similarity in amplitude is due to the motion along the field (latitude change of ∼13°) so that, despite the second being farther from the resonant shell, its amplitude remains comparable to the former. Segment 4 ends with the trace at a trough slightly before a trough in the guide signal.

Segment 5 shows the clear effect of the outer resonance outbound. The frequency increases due to the outbound spacecraft and inward phase motion. This increase is almost by a factor of two, as the trace completes a full cycle in only a half cycle of the guide.

Finally, in segment 6, the trace passes through zero at the time of a zero in the guide. From now on the effects of the resonances are over and the trace and the guide, having started in segment 1 in phase in the northern hemisphere, will oscillate in antiphase in the south (due to the standing structure along the field).

The orbit 'c' trace in the lower panel of Figure 6 has a strong resemblance to orbit 'b'. The major difference is that equatorial behavior is seen just after the innermost shell crossing. As the spacecraft encounters the equator at a different guide phase the wiggle is reversed. The outer resonance is not as clear inbound as on orbit 'b' (due to the resonance occurring essentially at the beginning of the trace), but it is clear outbound. The resonance effect is over by the final guide half cycle in the plot where the trace is now in antiphase with the guide. The segments 1–6 for orbit 'c' (lower panel) provide a similar picture to those for orbit 'b' (middle panel), as explained in detail in the previous paragraphs.

5.3. Meridional Components as a Metronome

The lower two panels of Figure 6 illustrate how the spatial structure of the phase across an FLR can cause a strong Doppler shift in the frequency measured on a spacecraft, if the transit time through the FLR is comparable with the wave period. As we have seen earlier, although both contain some spatial phase structure, the meridional magnetic field components, b_α and b_γ are dominated by the fast eigenmode global structure. The FLR represents a far smaller contribution to these components and therefore the resonance phase change effect on the b_α and b_γ signals is much smaller. Thus, although all three components have the same frequency in the plasma rest frame, on a moving spacecraft the resonant effect on the azimuthal b_β component can exhibit the frequency change associated with crossing the resonance, while the meridional components do not. This is illustrated in Figure 7. The top panel shows the transverse meridional component, b_α, and the lower panel shows the azimuthal magnetic field component, b_β, from orbit 'b' in Figure 5. Again, the blue portion is the inbound pass and the red portion is the outbound. The amplitudes of the two transverse components are very different (see scale on *y*-axes), something that gives a problem of detectability in the Cassini data. However, it is clear in the simulation that b_β exhibits a frequency change between inbound and outbound legs whereas b_α follows the guide sinusoid except for the abrupt change of sign across the equator. In this way, although the amplitude of the meridional component is much smaller, where detectable, it is a metronome indicating the frequency in the plasma rest frame.

6. Examples From the Cassini Spacecraft Proximal Orbits

The simulation results show that detecting the likely presence of resonances from a moving spacecraft in realistic conditions may be extremely difficult, particularly if the signal is highly azimuthally polarised and there is no information derivable from components little affected by resonance. The spatial variation in phase inherent to FLR in the rest frame of the plasma may be detected on a moving spacecraft as a variation in wave period. The standing structure along the background field also needs to be accounted for. For the fundamental, the transverse magnetic amplitude is expected to be antisymmetric in latitude. A high inclination orbit will detect a large latitudinal amplitude variation due to this and there should be a phase change of π between hemispheres. The resonance effect also depends on the time for spacecraft passage through the signal. A steep local gradient of the FLR frequency, ω_A, may mean that the resonance effect is no more than a jump in phase of π, but such a narrow resonance saturates at a smaller amplitude. As we have shown from the simulations, direction of travel with respect to the gradient, $d\omega_A/dL$ is important. In the situations modeled, where the spacecraft crosses the resonance inbound and then again outbound, the sense of the Doppler shift of the frequency induced by the FLR will be opposite.

The Doppler shift is downward (in frequency) where the gradient of the standing Alfvén eigenfrequency, ω_A, along the spacecraft track is negative and the shift is to a higher frequency when the gradient is positive. The examples of highly azimuthally polarised signals found by Southwood et al. (2021) come from a region on magnetic shells planetward of Saturn's rings where the spacecraft enters a region where the plasma density is enhanced. Thus, there should be a positive gradient of ω_A, (i.e., $d\omega_A/dL > 0$) as the spacecraft crosses the innermost ring, the D-ring. Once in the high-density region, ω_A might increase or decrease as the spacecraft comes closer to the planet. Unfortunately, the measurements of the mass and charge density on Cassini are confused by

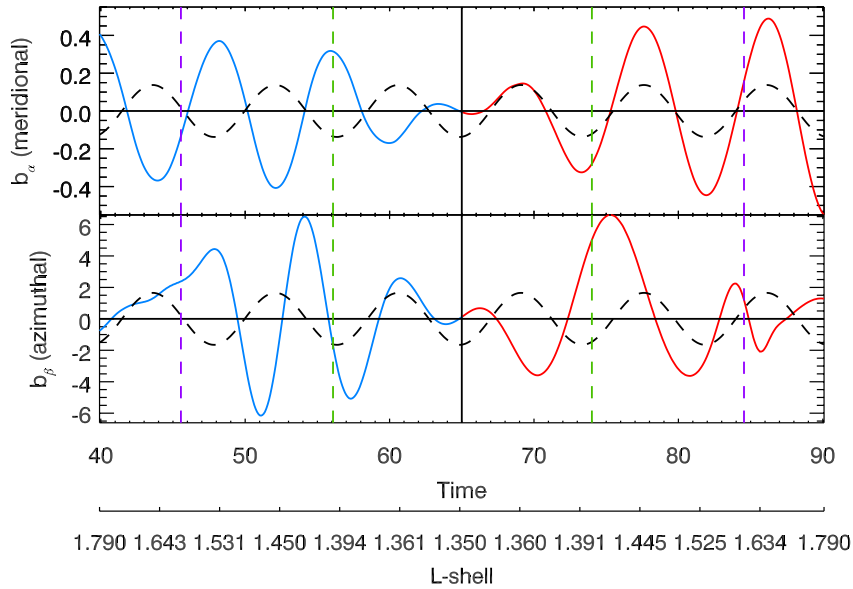

Figure 7. Meridional magnetic field b_α (top) and azimuthal magnetic field b_β (bottom) measured in time along the satellite trajectory labeled 'b' in Figure 5, which crosses the inner region field line resonance (FLR). Blue represents the inbound portion of the orbit, red the outbound. The vertical line gives the time when the orbit switches from inbound to outbound in L-shell, which coincides with crossing the magnetic equator. The purple/green dashed lines represent the times at which the two inner FLRs at $L = 1.6$/L = 1.4 are crossed.

the presence of charged dust (Morooka et al., 2019). In our computational model, we assumed $d\omega_A/dL < 0$ in this inner region (see Figure 2c). The observations we shall show indicate that the effective mass density controlling ω_A decreases with decreasing L.

The presence of signals in more than one frequency band confuses observations, particularly where the time of passage through the signal is a limited number of cycles. Southwood et al. (2021) dealt with this aspect by getting around the limitations on spectral analysis introduced by the finite time spent in the signal, by subtracting a cubic spline fit with a window near the expected lower frequency from the data. Details of this analysis procedure are provided in Section 2 of Southwood et al. (2021).

Our first example is from a Cassini pass, Rev 288, which provided one of the deepest penetrations of the planetary field. Data is shown in the two panels of Figure 8. 60-s averaged data from the residual signal left after subtracting a cubic spline with a 5 min window is used. In addition, the perturbation radial field in the lower panel has been obtained by subtracting the radial component of the C11 model planetary field (Dougherty et al., 2018). A total of 25 min (1,500 s) of data are shown taken on 14 August 2017 between 04:05:42 and 04:30:42. The plots are centered on the time of encounter with the innermost magnetic shell ($t = 0$).

The magnetic L shell parameter was derived from the C11 internal Saturn field model (Dougherty et al., 2018) and corresponds to the radial distance where a shell crosses the equatorial (ring) plane measured in R_s (Saturn radii). The model is axisymmetric with respect to the Saturn rotation axis and so shells are axisymmetric. Ancillary data indicating the local magnetic shell parameter, planetary latitude, and local time (LT) for the spacecraft location are given below the time axis in Figure 8. Due to the planetary field not being north-south symmetric and that the orbits are not strictly polar, on this pass the spacecraft crosses the point where the background field is horizontal (parallel to the surface of the planet) 104 s before the innermost shell encounter. We take this point as a proxy for the magnetic equator. Its location is shown by a light blue vertical line in each panel. The L shell parameter shows that at the same time before and after the innermost shell, the spacecraft encounters the same magnetic shell. This is indicated by the central lighter shaded region. The overall spacecraft motion is from north to south and during the 25 min shown the spacecraft crosses 1.5 hr of LT near the noon meridian.

The radial meridional component is shown in the lower panel and the azimuthal in the top. The amplitude scale differs between the two panels as the radial oscillation, ΔB_r is weaker. This is an unusual pass however in having a comparatively large radial signal. The ΔB_θ parallel component was too weak to provide a reliable signal and is

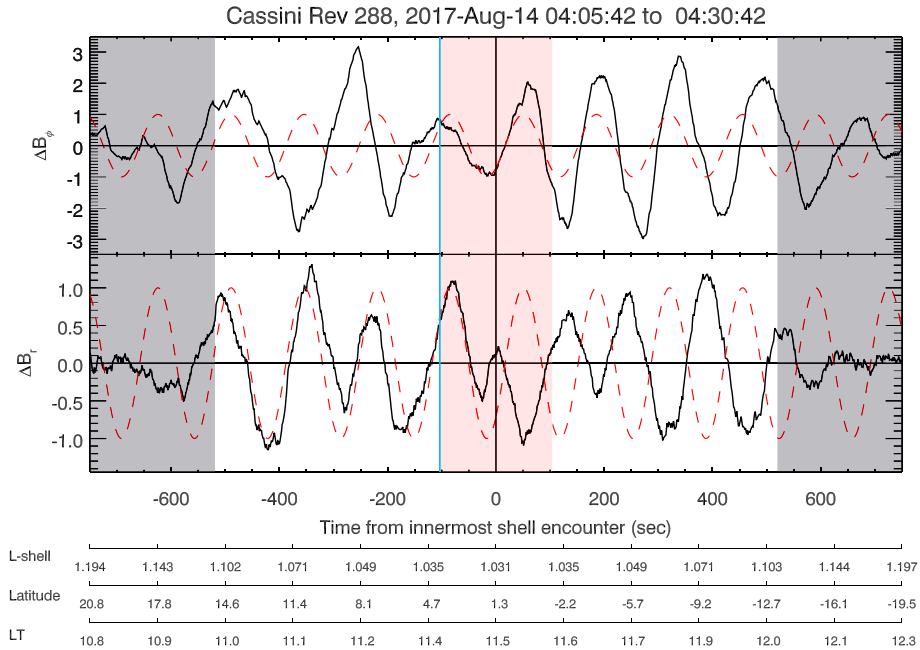

Figure 8. Azimuthal component, ΔB_ϕ, and radial component, ΔB_r, measured by the magnetometer on the Cassini spacecraft from Rev (orbit) 288 on 14 August 2017 04:05:42 to 04:30:42 UT. The data are in a band corresponding to 1–5 min, filtered by a procedure for separating into the two bands which is described by Southwood et al. (2021). The red dashed trace is a guide sinusoid with 135 s period. The light red shaded region ($-104 < T < 104$) begins where the spacecraft crosses the $B_r = 0$ point (magnetic proxy equator, marked with light blue vertical line) inbound and ends when the spacecraft attains the same L value outbound. The darker shaded regions on the extreme left and right represent where the spacecraft is on magnetic shells threading the innermost Saturn ring, the D-ring.

not shown. In each panel, black traces show the magnetic perturbations and red dashed traces are guide sinusoids with 135 s periods.

The scenario envisaged by Southwood et al. (2021) is that the meridional signal is associated with the global eigenmode and it is pumping locally the azimuthal signal associated with the Alfvén mode and FLR. The radial component in the bottom panel in the meridian fits quite well with the 135 s period guide trace inbound. The black trace of the component is close to being in phase with the guide sinusoid as the spacecraft comes inbound from the north. The phase relationship between ΔB_r then changes by π for the outbound leg in the southern hemisphere. This is consistent with there being a null in any transverse component near the equator in the fundamental wave structure as expected. All in all, the capacity to detect the meridional signal on this pass gives a clear idea of the pump frequency and this can now be compared to the larger amplitude azimuthal oscillations.

It is apparent that the black azimuthal component ΔB_ϕ trace in the top panel has a much less clear relationship to the sinusoidal red trace in the same panel. The signal is not coherent with the 135 s period guide trace. Looking to the extreme left and right, one sees that the first half cycle is approximately in phase with the red sinusoid and the last cycle is in antiphase with it. Thus, overall the phase of the ΔB_ϕ trace relative to the red guide signal has changed by π between inbound and outbound, in the same manner as for ΔB_r, due to the fundamental field-aligned mode structure.

Despite the irregularity of the signal, the number of peaks between $t = -500$ s and -100 s once planetward of the D-ring inbound on the pass is two, while outbound between 100 and 500s it is three, symptomatic of the difference in frequency between inbound and outbound. This is good evidence of the spacecraft encountering FLR behavior, similar to the model results presented in Figure 6. We can also deduce that the spacecraft is encountering an inward spatial variation in phase inbound (thereby increasing the observed period) and the opposite sense outbound (decreasing the observed period). The reversal of sense is predicted by the simulations but in the simulation, it was assumed the gradient was the opposite. Here, the Doppler shift to lower frequency on the inbound (left) pass and to higher frequency outbound (right) indicates that the Alfvén frequency, ω_A, decreases throughout

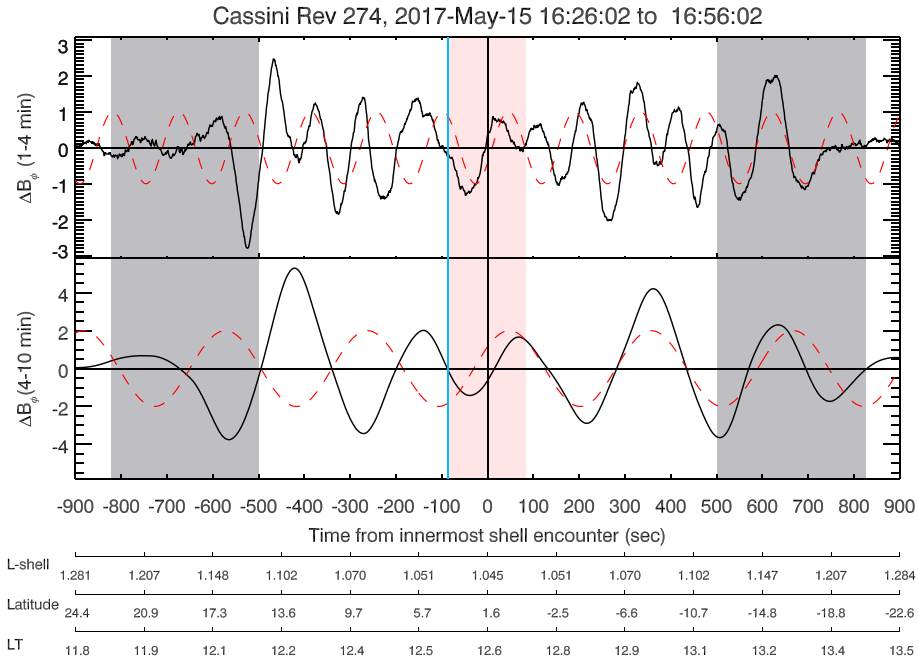

Figure 9. ΔB_ϕ measured by the magnetometer on the Cassini spacecraft from Rev (orbit) 274 on 15 May 2017 16:26 to 16:56 UT, filtered. Top panel shows the data filtered using a 1–4 min period filter, and the bottom panel 4–10 min periods. Red dashed traces are 144 and 310 s period sinusoids for guidance. The light red shaded region ($-87 < T < 87$) begins where the spacecraft crosses the $B_r = 0$ point (proxy equator) inbound and ends when the spacecraft attains the same shell outbound. The vertical light blue marker shows the equatorial point and one can see that in both bands there is a null in the field there, marking the phase change of π between the northern and southern hemispheres as expected for a fundamental wave structure. As shown in Figure 8, the darker shaded regions represent where the spacecraft is crossing the D-ring magnetic shells.

the region planetward of the D-ring and thus $d\omega_A/dL > 0$ throughout. As noted earlier, the absence of firm mass density measurements due to the presence of charged dust precludes direct checking.

In the Cassini spacecraft data, the amplitude of signals in the meridian is often too small to identify reliably. Figure 9 shows an instance where this is true. We show data from orbit Rev 274 illustrating the azimuthal signals in a high frequency 1–4 min period band in the upper panel and in the low frequency 4–10 min period band in the lower.

At first sight, the signal in the lower panel fits well with the red dashed sinusoid trace which has a period of 310 s. There is a reversal of sign (phase jump of π) across the equatorial region so that the black trace of the observed signal moves from being in anti-phase inbound to in-phase outbound. This kind of pattern is found often where there is a low frequency signal present. As the simulations have shown the amplitude variation can be attributed to the latitudinal variation through the fundamental mode structure along the field. There is very little phase difference with the 310 s guide trace and so there is no evidence of an FLR being crossed on the pass. On the right-hand side, the oscillations are slightly more rapid than on the left which can be attributed to a minor effect due to traveling through a gradient $d\omega_A/dL > 0$. Thus, the evidence from this panel indicates that the spacecraft may be traveling through a region where ω_A is varying but the spacecraft does not penetrate deep enough to encounter any FLR.

The high frequency signal in the top panel is more complicated. A guide red dashed sinusoid with period 144 s is shown. The black observed signal can be seen to change phase with respect to the guide trace by around π in the first cycles between −650 and −350s, and again by the half-cycle just before the equator at −100s. After the passage through the equatorial region after 100 s, the phase of the observed trace has changed by π and then it changes again by π before the cycles near 500–750s. Between −350 and −150s inbound there are ∼1.5 guide cycles but ∼2 trace cycles. Between 100 and 300s outbound, there are 2.5 trace cycles. Thus there are fewer oscillations inbound than outbound. We conclude that there is evidence for passage through an FLR in this band but that it is likely the inward plasma density gradient is also irregular.

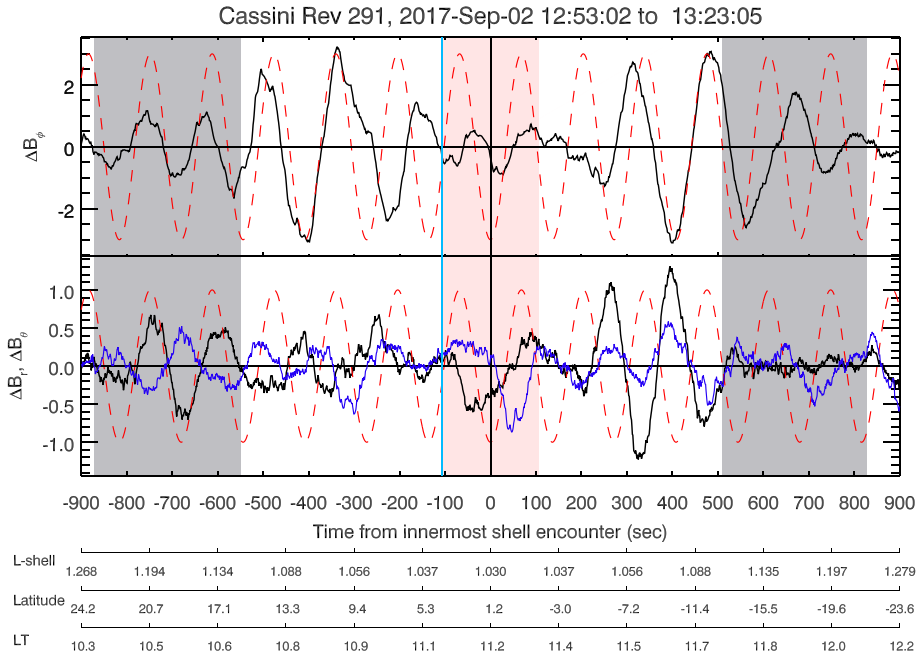

Figure 10. An example used by Southwood et al. (2021) detected on Cassini orbit, Rev 291 on 02 September 2017 between 12:53:02 and 13:23:05 UT. The *x*-axis is time, t, measured in seconds from when the spacecraft encounters the innermost magnetic shell (EqL = 1.03). The upper panel shows the perturbed ΔB_ϕ component and the lower panel shows the radial ΔB_r (black) and compressional ΔB_θ (blue) components. The procedure by which the signals are derived is described in the text. The red dashed line is a guide sinusoid with period 136 s. The magnetic equator inbound is shown by the light blue vertical line. The light red shaded section marks the equatorial region where the spacecraft is moving in and then out to the same magnetic shell as the equatorial crossing. The darker shaded regions represent crossing the D-ring shells.

Our interpretation assumes several signal features that we have assumed in the simulations. First, not only is there a fairly monochrome source at a large distance (e.g., as provided by a global eigenmode) but also the excitation source of the MHD waves is quasi-steady during the pass. In the example in the lower panel of Figure 8, the fairly regular nature of the signal detected in the meridional component supports the idea that there is steady excitation for the duration of the spacecraft pass. However, it cannot be guaranteed. In our final example we show a case where we have a detectable meridional signal, but which shows the excitation may be sporadic.

Figure 10 shows all three magnetic perturbation field components in spherical polar coordinates for Cassini Rev 291 on 2 September 2017 between 12:53:02 and 13:23:02 UT. The upper panel shows the azimuthal component with a black trace and a red dashed guide sinusoid with a 136 s period. The lower panel shows ΔB_r (black trace) and ΔB_θ (blue trace) as well as the same guide sinusoid with period 136 s (red dashed trace).

The lower panel exhibits irregular signals in the meridional components. However, there are packets with ∼136s period apparent inbound between −800s and around −450s and outbound between 250 and 600s. Within the packets, ΔB_r and ΔB_θ appear roughly in antiphase inbound and in phase outbound. This is consistent with signals having fundamental structure along the background field as although transverse components have a node at the equator, the compressional component ΔB_θ would have an antinode there. Between −450 and 250s and after 600s, it does not look as if the meridional components are oscillating coherently at 136s and so would not efficiently pump the FLR. Accordingly, in this example, there is no reason to assume an overall coherent response during the entire spacecraft passage. Indeed, the break in oscillations in ΔB_ϕ also is symptomatic of this being the case.

7. Final Remarks

Our work has well demonstrated an aspect of magnetospheric MHD waves that applies in any planetary environment. The field line resonance has some distinct properties. The most significant is the inherent spatial phase variation from magnetic shell to shell associated with field line resonance structure. The spatial phase change would be detected on a moving spacecraft as a frequency change in any circumstance. Although the total phase change

is at most π, if the time the spacecraft takes for crossing is comparable with the wave period, the change detected on the spacecraft is very substantial, increasing the apparent frequency by up to 50% or decreasing it by as much as a factor of 2. Figure S1 in Supporting Information S1 provides a visual confirmation of this effect. If the source is broad band the phase structure would produce a different effect. The frequency would show a monotonic apparent frequency increase as the spacecraft moves in one sense and a decrease as it moves in the other. It is important to note that such effects have been seen in the terrestrial magnetosphere (Anderson et al., 1989; Takahashi et al., 1990). The fact that we do not see evidence of such continuous change in frequency argues for the idea that the FLRs are being driven by fast MHD resonances of a larger magnetospheric cavity. The cavity might not be the entire Saturn magnetosphere but might be, for example, the low density plasma region planetward of the plasma torus originating from Enceladus.

To summarize and for ease of reference, the main findings are succinctly listed as follows:

- We have modeled observations of Alfvén waves from the proximal orbits of the Cassini spacecraft reported by Southwood et al. (2021). This has been achieved using a linear MHD wave model in a background dipole magnetic field geometry, specifically designed to resolve small perpendicular scales inherent in Alfvén wave phase mixing.
- The model raised several interesting features, most notably the phase motion associated with a field line resonance, with the direction of phase motion being determined by the Alfvén frequency gradient.
- Strong gradients in frequency imply smaller amplitude resonances, something which has been known for many years, however, is perhaps at first a counter-intuitive result (e.g., see the resonance amplitudes in the middle panel of Figure 3).
- By looking at virtual spacecraft orbits in the simulations, the importance of the phase motion on the spacecraft signal became apparent by the presence of a strong Doppler shift in the frequency. This was then shown to be a feature of the observations, which highlights the important relationship between observations and modeling.
- The simulations further reveal fundamental information about the coupling of a diffuse, larger outer cavity and a smaller dense inner cavity, which could have applications at Earth and other planets, for example, the coupling of the plasmasphere and outer magnetosphere through fast and Alfvén waves.
- The further observations presented here than in Southwood et al. (2021) validate the interpretation from that paper, of the driving of Alfvén waves at a consistent frequency provided by global modes of a larger magnetospheric cavity.

Appendix A: Derivation of Governing Equations Near Resonance

In this appendix, we provide a derivation of Equations 3 and 4 in the main body of the paper. These are derived from the two linearized equations of MHD that cover the relationship between the perturbed plasma displacement $\boldsymbol{\xi}$ and the associated magnetic field perturbation, $\boldsymbol{b}$, in a cold plasma. Assuming that all field components are proportional to $e^{-i\omega t}$, the pertinent linear equations can be written as:

$$-\mu_0\rho\omega^2\boldsymbol{\xi} = [(\boldsymbol{\nabla}\times\boldsymbol{b})\times\boldsymbol{B}], \tag{A1}$$

which is the equation of motion, and

$$\boldsymbol{b} = \boldsymbol{\nabla}\times(\boldsymbol{\xi}\times\boldsymbol{B}) \tag{A2}$$

is the induction equation where the frozen in flux condition (i.e., ideal MHD) has been assumed. Using the α, β, γ coordinates as used in the numerical model described in Section 2, the perturbation magnetic field can be expressed in the form

$$\boldsymbol{b} = b_\alpha h_\alpha \boldsymbol{\nabla}\alpha + b_\beta h_\beta \boldsymbol{\nabla}\beta + b_\gamma\left(\frac{\boldsymbol{B}}{B}\right), \tag{A3}$$

where h_α and h_β are the geometrical scale factors associated with the α and β coordinates respectively, which are defined through the background magnetic field as

$$\boldsymbol{B} = \boldsymbol{\nabla}\alpha\times\boldsymbol{\nabla}\beta = \frac{1}{h_\alpha h_\beta}\hat{\boldsymbol{\alpha}}\times\hat{\boldsymbol{\beta}}, \tag{A4}$$

where $\hat{\boldsymbol{\alpha}}$ and $\hat{\boldsymbol{\beta}}$ are the unit vectors in the α and β coordinate directions, which are transverse to the background magnetic field by definition. The scalar B in Equation A3 is the magnitude of $\boldsymbol{B}$. From the equation of motion Equation A1, it can be seen that the displacement $\boldsymbol{\xi}$ only has components perpendicular to $\boldsymbol{B}$. Therefore, we can write the displacement as

$$\boldsymbol{\xi} = \xi_\alpha h_\alpha \nabla\alpha + \xi_\beta h_\beta \nabla\beta. \tag{A5}$$

To simplify the algebra, we can consider how the different components of $\boldsymbol{b}$ contribute to Equation A1. Taking the β component of $\boldsymbol{b}$, the right hand side of Equation A1 is

$$\begin{aligned}\left[(\nabla \times b_\beta h_\beta \nabla\beta) \times \boldsymbol{B}\right] &= \left[\nabla(b_\beta h_\beta) \times \nabla\beta\right] \times \boldsymbol{B} \\ &= \boldsymbol{B} \cdot \nabla(b_\beta h_\beta)\nabla\beta\end{aligned} \tag{A6}$$

where in the first step we have used the vector identity $\nabla \times (f\boldsymbol{A}) = f\nabla\times\boldsymbol{A} + \nabla f \times \boldsymbol{A}$ for scalar f and vector $\boldsymbol{A}$. The vector triple product rule has then been applied to give the final form on the right hand side. Let us now consider the contribution of the γ component of $\boldsymbol{b}$ to Equation A1:

$$\begin{aligned}\left[\left(\nabla \times b_\gamma \frac{\boldsymbol{B}}{B}\right) \times \boldsymbol{B}\right] &= \left[\left(\frac{b_\gamma}{B}\right)\nabla \times \boldsymbol{B} + \nabla\left(\frac{b_\gamma}{B}\right) \times \boldsymbol{B}\right] \times \boldsymbol{B} \\ &= \left[\nabla\left(\frac{b_\gamma}{B}\right) \times \boldsymbol{B}\right] \times \boldsymbol{B},\end{aligned} \tag{A7}$$

upon using the same vector identity as used above for taking the curl of a scalar times a vector, together with assuming an irrotational or current free background field, such that $\nabla \times \boldsymbol{B} = 0$. The right hand side of Equation A7 can be simplified further using the vector triple product to give

$$\left[\nabla\left(\frac{b_\gamma}{B}\right) \times \boldsymbol{B}\right] \times \boldsymbol{B} = \left(\boldsymbol{B} \cdot \nabla\left(\frac{b_\gamma}{B}\right)\right)\boldsymbol{B} - B^2\nabla\left(\frac{b_\gamma}{B}\right) = -B^2\nabla_\perp\left(\frac{b_\gamma}{B}\right). \tag{A8}$$

Consider now the contribution of ξ_β to the right hand side of Equation A2:

$$\nabla \times (\xi_\beta h_\beta \nabla\beta \times \boldsymbol{B}) = \nabla \times \left[\xi_\beta h_\beta \nabla\beta \times (\nabla\alpha \times \nabla\beta)\right],$$

using the form of the background magnetic field given by Equation A4. Using the triple vector product rule and the orthogonality of $\nabla\alpha$ and $\nabla\beta$, it can be shown that

$$\begin{aligned}\nabla \times \left[\xi_\beta h_\beta \nabla\beta \times (\nabla\alpha \times \nabla\beta)\right] &= \nabla \times \left(\xi_\beta h_\beta (\nabla\beta)^2 \nabla\alpha\right) \\ &= \nabla \times \left(\frac{\xi_\beta}{h_\beta}\nabla\alpha\right), \\ &= \nabla\alpha \times \nabla\left(\frac{\xi_\beta}{h_\beta}\right)\end{aligned}$$

having used that $|\nabla\beta| = 1/h_\beta$. Further considering the component of this term in the $\nabla\beta$ direction by taking the dot product with $\nabla\beta$ gives

$$\begin{aligned}\nabla \times (\xi_\beta h_\beta \nabla\beta \times \boldsymbol{B}) \cdot \nabla\beta &= \left(\nabla\left(\frac{\xi_\beta}{h_\beta}\right) \times \nabla\alpha\right) \cdot \nabla\beta \\ &= (\nabla\alpha \times \nabla\beta) \cdot \nabla\left(\frac{\xi_\beta}{h_\beta}\right), \\ &= \boldsymbol{B} \cdot \nabla\left(\frac{\xi_\beta}{h_\beta}\right).\end{aligned} \tag{A9}$$

We can also pull out the component of the equation of motion (A1) in the $\nabla\beta$ direction by taking the dot product with $\nabla\beta$ to give

$$\begin{aligned}-\mu_0\rho\omega^2\boldsymbol{\xi} \cdot \nabla\beta &= [(\nabla \times \boldsymbol{b}) \times \boldsymbol{B}] \cdot \nabla\beta \\ \Rightarrow -\mu_0\rho\omega^2\left(\frac{\xi_\beta}{h_\beta}\right) &= (\boldsymbol{B} \cdot \nabla(b_\beta h_\beta)\nabla\beta) \cdot \nabla\beta - \left(B^2\nabla\left(\frac{b_\gamma}{B}\right)\right) \cdot \nabla\beta,\end{aligned}$$

where the right hand sides of Equations A6 and A8 have been used. It can be shown that the component of $\boldsymbol{b}$ in the $\nabla\alpha$ direction would not contribute to this, hence why we only considered the β and γ components previously. We can simplify further to give

$$-\mu_0\rho\omega^2\left(\frac{\xi_\beta}{h_\beta}\right) = \frac{1}{h_\beta^2}\boldsymbol{B}\cdot\boldsymbol{\nabla}(b_\beta h_\beta) - \frac{B^2}{h_\beta^2}\frac{\partial}{\partial\beta}\left(\frac{b_\gamma}{B}\right). \tag{A10}$$

The fact that $|\nabla\beta| = 1/h_\beta$ has been used together with the component form of the gradient operator in curvilinear coordinates. This gives an equation for ξ_β in terms of b_β, but this can be complemented by taking the dot product of Equation A2 with $\nabla\beta$ to give

$$\boldsymbol{b}\cdot\boldsymbol{\nabla}\beta = \boldsymbol{\nabla}\times(\boldsymbol{\xi}\times\boldsymbol{B})\cdot\boldsymbol{\nabla}\beta$$

It can be shown, in a similar fashion to the derivation of Equation A9, that the ξ_α component will not contribute to this term as it gives a term perpendicular to $\nabla\beta$. Therefore we can just consider the ξ_β contribution, which from Equation A9 gives

$$\begin{aligned} \boldsymbol{b}\cdot\boldsymbol{\nabla}\beta &= \boldsymbol{B}\cdot\boldsymbol{\nabla}\left(\frac{\xi_\beta}{h_\beta}\right), \\ \Rightarrow\frac{b_\beta}{h_\beta} &= \boldsymbol{B}\cdot\boldsymbol{\nabla}\left(\frac{\xi_\beta}{h_\beta}\right) \end{aligned} \tag{A11}$$

Equation A11 is Equation 4 from the main body of the study. Using this form for b_β, we can eliminate b_β from Equation A10 as

$$\begin{aligned} -\mu_0\rho\omega^2\left(\frac{\xi_\beta}{h_\beta}\right) &= -\frac{B^2}{h_\beta^2}\frac{\partial}{\partial\beta}\left(\frac{b_\gamma}{B}\right) + \frac{1}{h_\beta^2}\boldsymbol{B}\cdot\boldsymbol{\nabla}\left(h_\beta^2\boldsymbol{B}\cdot\boldsymbol{\nabla}\left(\frac{\xi_\beta}{h_\beta}\right)\right), \\ \Rightarrow -\mu_0\rho\omega^2\xi_\beta - \frac{1}{h_\beta}\boldsymbol{B}\cdot\boldsymbol{\nabla}\left(h_\beta^2\boldsymbol{B}\cdot\boldsymbol{\nabla}\left(\frac{\xi_\beta}{h_\beta}\right)\right) &= -\frac{B^2}{h_\beta}\frac{\partial}{\partial\beta}\left(\frac{b_\gamma}{B}\right). \end{aligned} \tag{A12}$$

Equation A12 has the familiar form of a driven harmonic oscillator, with the right hand side representing the driving term. Assuming that both ξ_β and b_β have a standing structure along the field, and considering only the free transverse oscillation in the absence of driving (i.e., the left hand side of Equation A12), we have

$$-\mu_0\rho\omega_A^2(\alpha)\xi_\beta - \frac{1}{h_\beta}\boldsymbol{B}\cdot\boldsymbol{\nabla}\left(h_\beta^2\boldsymbol{B}\cdot\boldsymbol{\nabla}\left(\frac{\xi_\beta}{h_\beta}\right)\right) = 0,$$

where the Alfvén frequency ω_A has been used for this transverse wave, on a particular magnetic shell labeled by α. Using this to substitute back into Equation A12 gives

$$\mu_0\rho\left[\omega_A^2(\alpha) - \omega^2\right]\xi_\beta = -\frac{B^2}{h_\beta}\frac{\partial}{\partial\beta}\left(\frac{b_\gamma}{B}\right). \tag{A13}$$

Introducing a uniform ion-neutral collision frequency, ν, to represent the effect of dissipation used in the simulations, yields

$$\xi_\beta = \frac{1}{\left(\omega^2 - \omega_A^2 + 2i\nu\omega\right)}\frac{B^2}{h_\beta\rho\mu_0}\frac{\partial}{\partial\beta}\left(\frac{b_\gamma}{B}\right), \tag{A14}$$

which is Equation 3 in the main body of the paper.

Data Availability Statement

The data used in this work are available from the NASA Planetary Data System: https://pds-atmospheres.nmsu.edu/data_and_services/atmospheres_data/Cassini/inst-mag.html. Data used to produce the simulation plots can be accessed at this site: https://figshare.com/authors/Tom_Elsden/4743264.

Acknowledgments
T. Elsden was funded by a Leverhulme Early Career Fellowship (ECF-2019-155), the University of Leicester and the University of Glasgow. D. Southwood acknowledges funding from UK Science and Technology Facilities Council Grant: ST/W001071/1.

References

Anderson, B. J., Engebretson, M. J., & Zanetti, L. J. (1989). Distortion effects in spacecraft observations of MHD toroidal standing waves: Theory and observations. *Journal of Geophysical Research*, *94*(A10), 13425–13445. https://doi.org/10.1029/JA094iA10p13425

Denton, R. E., Takahashi, K., Galkin, I. A., Nsumei, P. A., Huang, X., Reinisch, B. W., et al. (2006). Distribution of density along magnetospheric field lines. *Journal of Geophysical Research (Space Physics)*, *111*(A4), A04213. https://doi.org/10.1029/2005JA011414

Dougherty, M. K., Cao, H., Khurana, K. K., Hunt, G. J., Provan, G., Kellock, S., et al. (2018). Saturn's magnetic field revealed by the Cassini Grand Finale. *Science*, *362*(6410), aat5434. https://doi.org/10.1126/science.aat5434

Elsden, T., & Wright, A. N. (2015). The use of the Poynting vector in interpreting ULF waves in magnetospheric waveguides. *Journal of Geophysical Research (Space Physics)*, *120*(1), 166–186. https://doi.org/10.1002/2014JA020748

Elsden, T., & Wright, A. N. (2017). The theoretical foundation of 3-D Alfvén resonances: Time-dependent solutions. *Journal of Geophysical Research (Space Physics)*, *122*(3), 3247–3261. https://doi.org/10.1002/2016JA023811

Glassmeier, K.-H., & Espley, J. (2006). ULF waves in planetary magnetospheres. In: Magnetospheric ULF waves: Synthesis and new directions. *American Geophysical Union: Wiley*, *169*, 341–359. https://doi.org/10.1029/169GM22

Heilig, B., Sutcliffe, P. R., Ndiitwani, D. C., & Collier, A. B. (2013). Statistical study of geomagnetic field line resonances observed by CHAMP and on the ground. *Journal of Geophysical Research (Space Physics)*, *118*(5), 1934–1947. https://doi.org/10.1002/jgra.50215

Kageyama, A., Sugiyama, T., Watanabe, K., & Sato, T. (2006). A note on the dipole coordinates. *Computers & Geosciences*, *32*(2), 265–269. https://doi.org/10.1016/j.cageo.2005.06.006

Kivelson, M. G., & Southwood, D. J. (1985). Resonant ULF waves - a new interpretation. *Geophysical Research Letters*, *12*(1), 49–52. https://doi.org/10.1029/GL012i001p00049

Kivelson, M. G., & Southwood, D. J. (1986). Coupling of global magnetospheric MHD eigenmodes to field line resonances. *Journal of Geophysical Research*, *91*(A4), 4345–4351. https://doi.org/10.1029/JA091iA04p04345

Mann, I. R., Wright, A. N., & Cally, P. S. (1995). Coupling of magnetospheric cavity modes to field line resonances: A study of resonance widths. *Journal of Geophysical Research*, *100*(A10), 19441–19456. https://doi.org/10.1029/95JA00820

Morooka, M. W., Wahlund, J. E., Hadid, L. Z., Eriksson, A. I., Edberg, N. J. T., Vigren, E., et al. (2019). Saturn's dusty ionosphere. *Journal of Geophysical Research (Space Physics)*, *124*(3), 1679–1697. https://doi.org/10.1029/2018JA026154

Newton, R. S., Southwood, D. J., & Hughes, W. J. (1978). Damping of geomagnetic pulsations by the ionosphere. *Planetary and Space Science*, *26*(3), 201–209. https://doi.org/10.1016/0032-0633(78)90085-5

Ozeke, L. G., Mann, I. R., & Mathews, J. T. (2005). The influence of asymmetric ionospheric Pedersen conductances on the field-aligned phase variation of guided toroidal and guided poloidal Alfvén waves. *Journal of Geophysical Research (Space Physics)*, *110*(A8), A08210. https://doi.org/10.1029/2005JA011167

Samson, J. C., Harrold, B. G., Ruohoniemi, J. M., Greenwald, R. A., & Walker, A. D. M. (1992). Field line resonances associated with MHD waveguides in the magnetosphere. *Geophysical Research Letters*, *19*(5), 441–444. https://doi.org/10.1029/92GL00116

Shi, X., Baker, J. B. H., Ruohoniemi, J. M., Hartinger, M. D., Murphy, K. R., Rodriguez, J. V., et al. (2018). Long-lasting poloidal ULF waves observed by multiple satellites and high-latitude SuperDARN radars. *Journal of Geophysical Research (Space Physics)*, *123*(10), 8422–8438. https://doi.org/10.1029/2018JA026003

Southwood, D. J. (1974). Some features of field line resonances in the magnetosphere. *Planetary and Space Science*, *22*(3), 483–491. https://doi.org/10.1016/0032-0633(74)90078-6

Southwood, D. J. (1975). Interpretation of apparent phase motion in micropulsation signals. *Geophysical Research Letters*, *2*(11), 483–484. https://doi.org/10.1029/GL002i011p00483

Southwood, D. J., Cao, H., Shebanits, O., Elsden, T., Hunt, G. J., & Dougherty, M. K. (2021). Discovery of Alfvén waves planetward of Saturn's rings. *Journal of Geophysical Research (Space Physics)*, *126*(2), e28473. https://doi.org/10.1029/2020JA028473

Southwood, D. J., & Kivelson, M. G. (2000). Relationships between phase structure and energy flux in magnetohydrodynamic waves in the magnetosphere. *Journal of Geophysical Research*, *105*(A12), 27701–27706. https://doi.org/10.1029/2000JA000261

Stewart, B. (1861). On the great magnetic disturbance which extended from August 28 to September 7, 1859, as recorded by photography at the Kew observatory. *Philosophical Transactions of the Royal Society of London,Series A I*, *151*, 423–430.

Takahashi, K., Anderson, B. J., & Strangeway, R. J. (1990). AMPTE CCE observations of Pc 3-4 pulsations at L=2-6. *Journal of Geophysical Research*, *95*(A10), 17179–17186. https://doi.org/10.1029/JA095iA10p17179

Takahashi, K., Denton, R. E., Anderson, R. R., & Hughes, W. J. (2006). Mass density inferred from toroidal wave frequencies and its comparison to electron density. *Journal of Geophysical Research (Space Physics)*, *111*(A1), A01201. https://doi.org/10.1029/2005JA011286

Vellante, M., Lühr, H., Zhang, T. L., Wesztergom, V., Villante, U., de Lauretis, M., & Magnes, W. (2004). Ground/satellite signatures of field line resonance: A test of theoretical predictions. *Journal of Geophysical Research (Space Physics)*, *109*(A6), A06210. https://doi.org/10.1029/2004JA010392

Wright, A. N., & Elsden, T. (2016). The theoretical foundation of 3D Alfvén resonances: Normal modes. *The Astrophysical Journal*, *833*(2), 230. https://doi.org/10.3847/1538-4357/833/2/230

Wright, A. N., & Elsden, T. (2020). Simulations of MHD wave propagation and coupling in a 3-D magnetosphere. *Journal of Geophysical Research (Space Physics)*, *125*(2), e27589. https://doi.org/10.1029/2019JA027589